also been obtained from these data. The three skewness factor profiles are shown in Fig. 3a with the same peak and valley profile shifts as described earlier. The smooth-plate profiles agree well with most data in the literature except that the values for the three locations nearest the wall appear to be somewhat too large because of wall proximity effects (see Alfredsson et al.[16]). At $y/\delta = 0.02$, the skewness factor increases dramatically spanwise from the peak to the valley. The smooth-plate skewness factor values lie between these two extremes. At about $y/\delta \geq 0.04$, the unshifted data collapse approximately to a single curve, indicating that the effects of the riblets on this statistic are confined to the region very close to the surface. This was also seen in Fig. 1a for the mean velocities. The flatness factors above the three surfaces are shown in Fig. 3b and exhibit similar trends. For the unshifted flatness factor profiles, above $y/\delta = 0.04$ all of the data collapse to a single curve.

The extremely large positive skewness and flatness values seen in Figs. 3a and 3b in the riblet valley around the midlevel ($y/\delta \approx 0.02$), when considered together with the small turbulence intensity values in that region in Fig. 2, indicate rare but large amplitude positive streamwise velocity fluctuations due to occasional penetration of fluid from higher in the flow. Below the midlevel, however, the intensity and the skewness and flatness factors in the valley decrease precipitously, showing that the streamwise velocity fluctuations there are almost symmetric and of extremely small magnitude deep within the grooves.

IV. Conclusions

The effects of the riblet surface on the mean and fluctuating streamwise velocity field are clearly exhibited in the $R_\theta \approx 10^3$ boundary-layer data shown earlier. The most dramatic effects are confined to within about 4% of the boundary layer above the riblets measured from the midlevel of the grooves. The local wall shear stress varies greatly in the spanwise direction, from about 85% greater than the smooth-plate value at the riblet peak for flow with the same freestream velocity, to vanishingly small at the riblet valley. The turbulence intensities and skewness and flatness factors of the streamwise velocity fluctuations all indicate that the turbulence nearly vanishes below the midlevel of the grooves. Occasionally, relatively large positive streamwise fluctuations occur in the region between the midlevel and peak of the grooves due to the penetration of the higher velocity fluid from above. However, unlike the vertical momentum transport over the smooth surface, this high momentum fluid rarely gets close to the riblet surface except near the peaks. Thus, the wall stress is lower than the flat-plate value over much of the span. When the resulting spanwise average shear stress is sufficiently lower than that for the smooth plate, more than compensating for the increased wetted surface area of the riblets, net drag reduction occurs.

References

[1]McLean, J. D., George-Falvy, D. N., and Sullivan, P. P., "Flight-Test of Turbulent Skin-Friction Reduction by Riblets," *Turbulent Drag Reduction by Passive Means,* Vol. II, Proceedings of the Royal Aeronautical Society, London, Sept. 1987, pp. 408–424.

[2]Walsh, M. J., and Weinstein, L. M., "Drag and Heat Transfer on Surfaces with Small Longitudinal Fins," AIAA Paper 78-1161, July 1978.

[3]Walsh, M. J., "Drag Characteristics of V-Groove and Transverse Curvature Riblets," *Viscous Drag Reduction,* edited by G. R. Hough, Vol. 72, Progress in Astronautics and Aeronautics, AIAA, New York, 1980, pp. 168–184.

[4]Walsh, M. J., "Turbulent Boundary Layer Drag Reduction Using Riblets," AIAA Paper 82-0169, Jan. 1982.

[5]Walsh, M. J., "Riblets as a Viscous Drag Reduction Technique," *AIAA Journal,* Vol. 21, No. 4, 1983, pp. 485, 486.

[6]Walsh, M. J., and Lindemann, A. M., "Optimization and Application of Riblets for Turbulent Drag Reduction," AIAA Paper 84-0347, Jan. 1984.

[7]Bechert, D. W., Hoppe, G., and Reif, W.-E., "On the Drag Reduction of Shark Skin," AIAA Paper 85-0546, March 1985.

[8]Nitschke, P., "Experimental Investigation of Turbulent Flow in Smooth and Longitudinal Grooved Tubes," NASA TM 77480, May 1984.

[9]Wallace, J. M., and Balint, J.-L., "Viscous Drag Reduction Using Streamwise Aligned Riblets: Survey and New Results," *Turbulence Management and Relaminarization,* edited by H. W. Liepmann and R. Narasimha, Springer-Verlag, Berlin, 1987, pp. 132–147.

[10]Purtell, L. P., Klebanoff, P. S., and Buckley, F. T., "Turbulent Boundary Layer at Low Reynolds Number," *Physics of Fluids,* Vol. 24, No. 5, 1981, pp. 802–811.

[11]Bacher, E. V., and Smith, C. R., "A Combined Visualization-Anemometry Study of the Turbulent Drag Reducing Mechanisms of Triangular Micro Groove Surface Modifications," AIAA Paper 85-0548, March 1985.

[12]Choi, K.-S., "Near-Wall Structure of a Turbulent Boundary Layer with Riblets," *Journal of Fluid Mechanics,* Vol. 208, 1989, pp. 417–458.

[13]Hooshmand, A., "An Experimental Investigation of the Influence of a Drag Reducing, Longitudinally Aligned, Triangular Riblet Surface on the Velocity and Streamwise Vorticity Fields of a Zero-Pressure Gradient Turbulent Boundary Layer," Ph.D. Dissertation, Dept. of Mechanical Engineering, Univ. of Maryland, College Park, MD, 1985.

[14]Weidman, P. D., and Browand, F. K., "Analysis of a Simple Circuit for Constant Temperature Anemometry," *Journal of Physics E,* Vol. 8, No. 7, 1975, pp. 553–560.

[15]Bechert, D. W., Bartenwerfer, M., and Hoppe, G., "Drag Reduction Mechanisms Derived from Shark Skin," *15th Congress, International Council for Aeronautical Sciences,* Paper 86-1.8.3, London, England, UK, Sept. 1986.

[16]Alfredsson, P. H., Johansson, A. V., Haritonidis, J. H., and Eckelmann, H., "The Fluctuating Wall-Shear Stress and the Velocity Field in the Viscous Sublayer," *Physics of Fluids,* Vol. 31, No. 5, 1988, pp. 1026–1033.

Use of Finite Volume Schemes for Transition Simulation

Charles C. Fenno Jr.*
North Carolina State University, Raleigh, North Carolina 27695
Craig L. Streett†
NASA Langley Research Center, Hampton, Virginia 23665
and
H. A. Hassan‡
North Carolina State University, Raleigh, North Carolina 27695

Introduction

THE efficient design of aerospace vehicles requires an understanding and appreciation for the many factors affecting the vehicle's performance. One of the more significant of these factors is the transition of a moving fluid from a smooth, laminar state to one of turbulence. The control of this

Received Oct. 29, 1990; presented as Paper 91-0743 at the AIAA 29th Aerospace Sciences Meeting, Reno, NV, Jan. 7–10, 1991; revision received July 18, 1991; accepted for publication July 18, 1991.

*Research Assistant, Mechanical and Aerospace Engineering. Student Member AIAA.

†Research Scientist, Theoretical Flow Physics Branch, Fluid Dynamics Division. Member AIAA.

‡Professor, Mechanical and Aerospace Engineering. Associate Fellow AIAA.

transition can lead to such things as reduced skin friction and improved surface heating characteristics. Yet as significant as transition's effects are, the underlying mechanisms of its causes have eluded theoretical description for over a century.

Direct numerical simulations of the transition process have been achieved by several authors (see, e.g., Refs. 1-5). Most of the computational work to date has relied heavily on spectral methods and addressed temporal effects only. However, due to the difficulties encountered when using spectral methods for solutions with discontinuities, as in compressible flows and for flows over realistic geometries, interest has risen for developing other numerical approaches that may be used in studying the mechanisms of transition. Typical of these are fourth-order methods.[6,7] However, such methods have not been applied to complex geometries. Unless fourth-order methods extend to the calculation of the metrics, fourth-order accuracy cannot be maintained.

The objective of this work is to use finite volume methods that are widely used for computational fluid dynamics (CFD) in studying spatially and temporally evolving transitional flows. The first test for such approaches is the ability to predict the locations of branch 1 and branch 2 of the neutral stability curves for subsonic and supersonic flows over a flat plate. To achieve this goal, schemes are developed with both central and upwind differencing. The compressible Navier-Stokes equations are solved with a Runge-Kutta time-stepping scheme. Disturbances are determined using linear theory and superimposed at the inflow boundary. Time-accurate integration is then used to allow temporal and spatial disturbance evolution. Characteristic-based boundary conditions are employed. Special emphasis is placed on determining grid and initial disturbance amplitude requirements for such simulations.

The second-order-accurate central differencing follows the approach of Jameson et al.[8] and uses fourth difference explicit damping. Use of such damping is not necessary when the Reynolds number is of the order of 10^4. However, it is necessary when Re is 10^6 or higher in order to control odd-even decoupling. When using such damping, one must insure that it does not affect the skin-friction coefficient. Roe's upwind scheme[9] is also used with accuracy of third order, i.e. $\kappa = -\frac{1}{3}$.

Procedure

The application of the method to the transition problem involves three basic steps. The first is to compute a mean flow. For this part of the calculation, temporal accuracy is not needed and the integration is used only to achieve a steady-state solution. It is extremely important that, for the high Reynolds number employed, a solution with smooth second derivatives be obtained.[10] Once the mean flow is obtained, the most amplified mode of the disturbance is determined from linear stability theory. A linear theory code developed by Macaraeg et al.[10] is used for this part of the procedure. This code solves the compressible linearized disturbance equations using a spectral technique, with the mean flow of the present method as input. Solutions to this eigenvalue problem yield the desired disturbance, written as

$$q'(x,y,z,t) = \tilde{q}(y)e^{i(\alpha x - \omega t)} \tag{1}$$

In Eq. (1), x is the coordinate in the streamwise direction, y is normal to the wall, and t is time. The vectors q' and $\tilde{q}$ represent the primitive variables: temperature, pressure, and velocity. The eigenvalues are the wave number α, the flow Reynolds number based on displacement thickness Re_{δ^*}, and the complex frequency ω. The linear theory code determines the most unstable frequency and the eigenfunctions $\tilde{q}$. Only the real part of the complex disturbance has physical significance and is used.

The third and final step involves superimposing the disturbance on the mean flow at the inflow boundary of the computation domain. Thus, a disturbed property q is written as

$$q = Q_0 + q' \tag{2}$$

where Q_0 represents the mean flow profile. The governing equations are then integrated in a time-accurate manner, allowing the disturbance to continually propagate into the flow. Once the disturbance has penetrated the entire field and moved through the outflow boundary, sampling of the desired properties is performed.

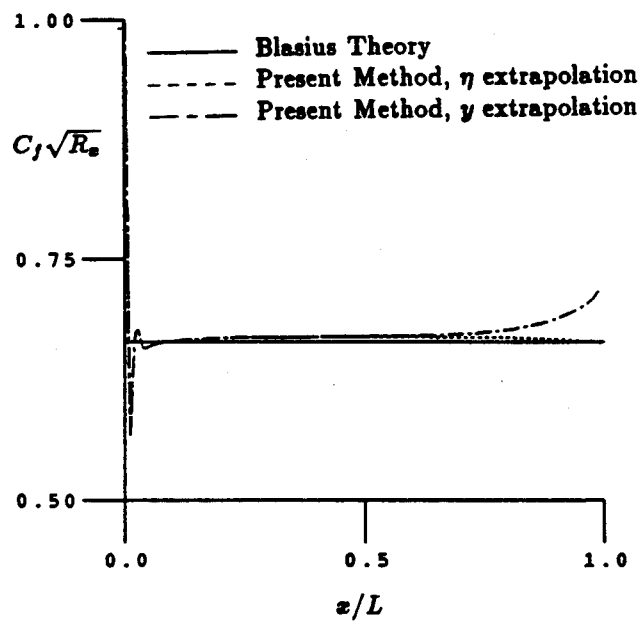

Fig. 1 Skin-friction parameter vs streamwise coordinate at $M = 0.3$ and $Re_L = 1 \times 10^6$.

Table 1 Critical points and amplifications ($M = 0.3$)

	Branch I, $\sqrt{Re_x}$	Branch II, $\sqrt{Re_x}$	Amplification, (A_{II}/A_I)
Linear theory ($M = 0$)	466	816	9.48
Spectral ($M = 0$)	468	813	9.26
Spectral ($M = 0.3$)	451	791	—
Case 1[a]	508	799	3.46
Case 2[b]	511	809	3.66
Case 3[c]	509	815	4.33
Case 4[d]	511	796	2.87
Case 5[e]	539	882	6.20

[a]Case 1: upwind difference, grid = 1200 × 38.
[b]Case 2: upwind difference, grid = 1200 × 82.
[c]Case 3: upwind difference, grid = 1800 × 82.
[d]Case 4: upwind difference, grid = 1050 × 38.
[e]Case 5: central difference, grid = 1050 × 38.

Results and Discussion

The results of varying the outflow boundary condition are shown in Fig. 1. The grid contained 220 × 38 cells and extended 10% of the plate length upstream of the leading edge. The mean flow case shown was for a Mach number of 0.3 and a Reynolds number based on the plate length of 1×10^6. The results are given in terms of the skin-friction parameter $C_f\sqrt{Re_x}$ vs the streamwise coordinate x/L, where C_f is the skin-friction coefficient. The cases of extrapolating the flow properties along the Cartesian grid lines and along a constant value of the Blasius similarity parameter η are compared with the Blasius theory. Much better agreement with the theory is seen for the extrapolation along the η lines, especially in the last 30% of the plate, indicating the importance of the downstream boundary condition. This is particularly important since the mean flow provides the basis of the time-accurate disturbance calculations. No special precautions were employed at the leading edge. Moreover, all subsequent calcula-

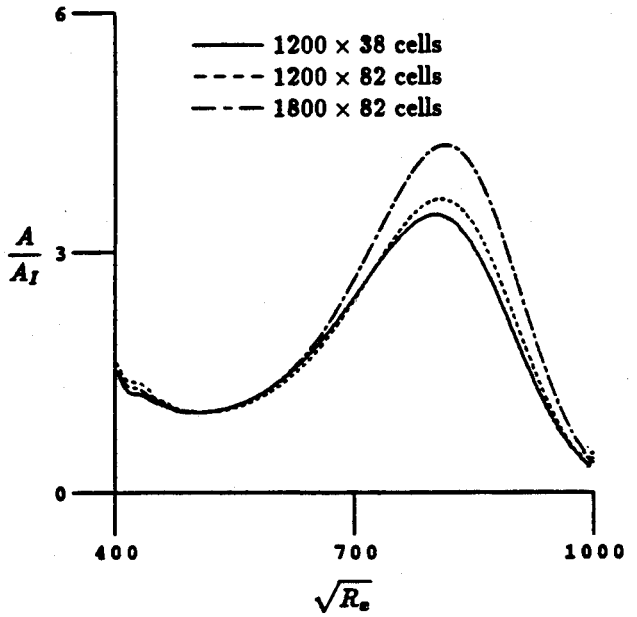

Fig. 2 Maximum streamwise velocity disturbance fluctuation vs Reynolds number at $M = 0.3$ and $\alpha = 0.3/\delta^*$ for different grids using upwind differencing.

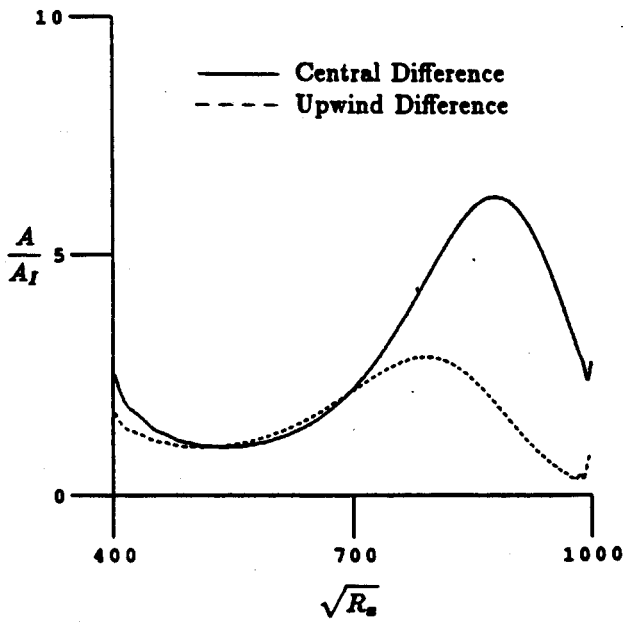

Fig. 3 Maximum streamwise velocity disturbance fluctuation vs Reynolds number at $M = 0.3$ and $\alpha = 0.17/\delta^*$ for upwind and central differencing on a 1050 × 38 grid.

tions used a steady solution appropriate for a semi-infinite flat plate.

The present work models a vibrating ribbon experiment that imposes a disturbance directly into the boundary layer, as opposed to natural receptivity in which a disturbance exists in the exterior flow and enters the viscous layer by natural means. The square root of the inflow Reynolds number based on x, $\sqrt{Re_x}$ was 4×10^2, whereas the outflow $\sqrt{Re_x}$ was 10^3. The nondimensional frequency of the disturbance is defined as

$$F = \frac{\omega_{Re}\nu}{U_\infty^2} \tag{3}$$

where ω_{Re} is the real part of ω, ν the kinematic viscosity, and U_∞ the freestream velocity. This nondimensional frequency was chosen as 86×10^{-6}. According to linear stability theory, for this frequency and range of Reynolds numbers, regions of stable and unstable flow should exist. The boundary where the flow initially becomes unstable is known as branch 1 of the neutral stability curve, whereas the boundary where it returns to a stable condition is known as branch 2. Cases were considered at a freestream Mach number of 0.3. A small amplitude disturbance of $\epsilon = 10^{-4}$ was used, where ϵ is the maximum amplitude of the input disturbance normalized by the freestream velocity. Figure 2 shows the effects of grid resolution. As may be seen from the figure, grid refinement affects the amplification but not the location of the critical points. The grids used provided from 35 to 52 cells per disturbance wavelength.

Next, comparison was made between using central differencing and upwind differencing for the spatial discretization, with the results shown in Fig. 3. The code developed for the present method ran at a speed of 6×10^{-6} CPU s/grid point/time step on a Cray Y-MP for the central difference scheme as compared to 12×10^{-6} CPU s for the upwind difference scheme. The two cases shown were calculated on a 1050×38 grid. The fourth-difference explicit damping coefficient for the central difference case was 3.125×10^{-3}. Both of the critical points for the central difference case were farther aft than for the upwind case, and the amplification for this case was much higher. This indicates that, although the central difference case requires the addition of explicit damping, the overall dissipation was less than the upwind method provided.

Table 1 gives a summary of the subsonic cases and compares them with the results of linear theory and a spectral/spatial simulation scheme.[11] The branch 1 points in all cases fell aft of the theoretical and spectral results, with the worst case being the central difference value of $\sqrt{Re_x} = 5.39 \times 10^2$. All of the upwind cases predicted the branch 2 point within 3.1%. The worst prediction for the branch 2 point was from the central difference calculation. Also shown in the table are the total amplifications between the two branches, with higher values seen for finer grids and for the central difference calculation.

The final case investigated a supersonic flow at $M = 1.6$. Figure 4 shows the fluctuations of the momentum variable ρu for central and upwind differencing. Because of the shifted area of unstable flow, as predicted by theory for this compressible case, the domain was set from $\sqrt{Re_x} = 2 \times 10^2$ to 7×10^2. The grid was 572×38 cells, resulting in 44 cells per disturbance wavelength. The central difference results are shown for two cases. The first is with $\epsilon^{(4)} = 5 \times 10^{-3}$, where $\epsilon^{(4)}$ is the fourth-order explicit damping coefficient. The second case is with an increase of 25% to $\epsilon^{(4)} = 6.25 \times 10^{-3}$. Generally, the same trends are seen as in Fig. 3, with greater amplification and critical points farther aft resulting from the central difference calculation.

Table 2 gives a summary for the supersonic cases. Also shown for comparison are results obtained from solutions of the parabolic stability equations (PSE) by Bertolotti.[12] The PSE are a numerically efficient equation set obtained after making simplifying assumptions to the Navier-Stokes equations. As a result of these assumptions, the solution may be marched in the streamwise direction. The critical points predicted by the Navier-Stokes methods were all forward of those

Table 2 Critical points and amplifications based on ρu fluctuations ($M = 1.6$)

	Branch I, $\sqrt{Re_x}$	Branch II, $\sqrt{Re_x}$	Amplification, (A_{II}/A_I)
PSE[a] method	361	580	1.290
Case 1[b]	311	498	1.632
Case 2[c]	311	497	1.612
Case 3[d]	306	480	1.418

[a]PSE = parabolic stability equations.
[b]Case 1: central difference, $\epsilon^{(4)} = 5.00 \times 10^{-3}$.
[c]Case 2: central difference, $\epsilon^{(4)} = 6.25 \times 10^{-3}$.
[d]Case 3: upwind difference.

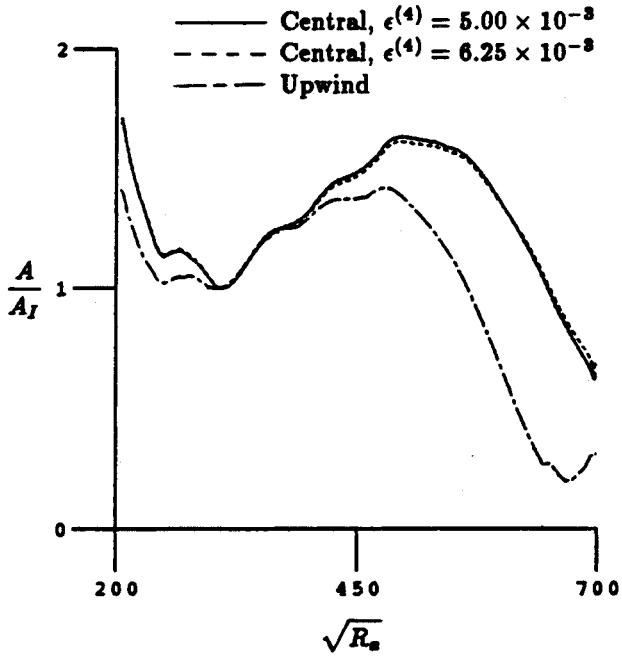

Fig. 4 Maximum streamwise momentum disturbance fluctuation vs Reynolds number at $M = 1.6$ and $\alpha = 0.11/\delta^*$ for upwind and central differencing on a 572 × 38 grid.

predicted by the PSE. The PSE also predicted a lower amplification than the present methods.

In conclusion, the requirements of two finite volume schemes as applied to the problem of fluid transition have been investigated. Calculations have been performed in both the subsonic and supersonic regimes. These schemes have been shown to be capable of predicting regions of stable and unstable flow that agree reasonably well with linear theory for low-amplitude disturbances. However, the resolution required to obtain useful results is somewhat high due to the level of accuracy of the numerical methods. Thus, there is a need to employ more accurate methods.

Acknowledgments

This work is supported in part by NASA's Cooperative Agreement NCCI-22, the Hypersonic Aerodynamic Program Grant NAGW-1022 funded jointly by NASA, the Air Force Office of Scientific Research, and the Office of Naval Research, and the Mars Mission Research Center funded by NASA Grant NAGW-1331. Some of the computer time was provided by the North Carolina Supercomputing Center.

References

[1]Wray, A., and Hussaini, M. Y., "Numerical Experiments in Boundary-Layer Stability," *Proceedings of the Royal Society of London,* Vol. A392, 1984, pp. 373–389.

[2]Zang, T. A., and Hussaini, M. Y., "Numerical Simulation of Nonlinear Interactions in Channel and Boundary-Layer Transition," *Nonlinear Wave Interactions in Fluids,* edited by R. W. Miksad, T. R. Akylas, and T. Herbert, ASME-AMD, Vol. 87, 1987, pp. 131–145.

[3]Laurien, E., and Kleiser, L., "Numerical Simulation of Boundary-Layer Transition and Transition Control," *Journal of Fluid Mechanics,* Vol. 199, 1989, pp. 403–440.

[4]Fasel, H. F., Rist, U., and Konzelmann, U., "Numerical Investigation of the Three-Dimensional Development in Boundary-Layer Transition," *AIAA Journal,* Vol. 28, No. 1, 1990, pp. 29–37.

[5]Spalart, P. R., and Yang, K., "Numerical Study of Ribbon-Induced Transition in Blasius Flow," *Journal of Fluid Mechanics,* Vol. 178, 1987, pp. 345–365.

[6]Bayliss, A., Parikh, P., Maestrello, L., and Turkel, E., "A Fourth-Order Scheme for the Unsteady Compressible Navier-Stokes Equations," AIAA Paper 85-1694, July 1985.

[7]Lele, S. K., "Direct Numerical Simulation of Compressible Free Shear Flows," AIAA Paper 89-0374, Jan. 1989.

[8]Jameson, A., Schmidt, W., and Turkel, E., "Numerical Solutions of the Euler Equations by Finite Volume Methods Using Runge-Kutta Time-Stepping Schemes," AIAA Paper 81-1259, 1981.

[9]Roe, P. L., "Characteristic-Based Schemes for the Euler Equations," *Annual Review of Fluid Mechanics,* Vol. 18, 1986, pp. 337–365.

[10]Macaraeg, M. G., Streett, C. L., and Hussaini, M. Y., "A Spectral Collocation Solution to the Compressible Stability Eigenvalue Problem," NASA TP-2858, 1988.

[11]Streett, C. L., and Macaraeg, M. G., "Spectral Multi-Domain For Large-Scale Fluid Dynamic Simulations," *Applied Numerical Mathematics,* Vol. 6, 1989, pp. 123–139.

[12]Bertolotti, F. P., "Linear and Nonlinear Stability of Boundary Layers with Streamwise Varying Properties," Ph.D. Dissertation, Ohio State Univ., Columbus, OH, 1990.

Freestream Capturing for Moving Coordinates in Three Dimensions

Shigeru Obayashi*
NASA Ames Research Center,
Moffett Field, California 94035

Introduction

BODY-CONFORMING coordinate transformations of a fluid conservation law are generally used in computational fluid dynamics. The associated metrics must satisfy certain geometric identities to maintain the global conservation for numerical solutions.[1] These metrics are called freestream capturing (or preserving) metrics. Numerical techniques are known to capture the freestream on stationary grids.[2-4] However, the extension of such a formulation for moving grids is not straightforward. The error introduced in forming the time metrics has been overlooked because it is negligible in most cases, but it can be significant in certain applications such as helicopter rotor flows.[5] Rigorous formulations based on the types of grid motions were discussed in Ref. 1, and demonstrated, for example, in Ref. 6. The present study describes detailed formulas that can be used in both finite volume (FV) and finite difference (FD) methods for constructing freestream capturing metrics in space and time.

Finite Volume Formulation

Geometric Identities and Freestream Capturing

The integral form of a conservation law for a given cell can be written as

$$\int_{V(t_2)} Q\,\mathrm{d}V - \int_{V(t_1)} Q\,\mathrm{d}V + \int_{t_1}^{t_2} \oint_{S(t)} \boldsymbol{n}\cdot\boldsymbol{F}\,\mathrm{d}S\,\mathrm{d}t = 0 \qquad (1)$$

where $V(t)$ is the cell volume and $\boldsymbol{n}\,\mathrm{d}S(t)$ is a vector element of surface area with outwardly normal $\boldsymbol{n}$. Considering the Euler equations, Q is a vector of conserved variables, viz., density, momentum, and energy, and $\boldsymbol{F}$ is the flux tensor of Q. The flux $\boldsymbol{F}$ can be decomposed into the flux in the stationary frame $\boldsymbol{F}_{\mathrm{st}}$ and the contribution due to surface element velocity $\boldsymbol{v}$ as

$$\boldsymbol{F} = \boldsymbol{F}_{\mathrm{st}} - \boldsymbol{v}Q \qquad (2)$$

Received Nov. 27, 1990; revision received June 10, 1991; accepted for publication June 24, 1991.

*Senior Research Scientist, MCAT Institute, San Jose, CA 95127.